Solar Energy 300 (2025) 113852

Contents lists available at ScienceDirect

Solar Energy

journal homepage: www.elsevier.com/locate/solener

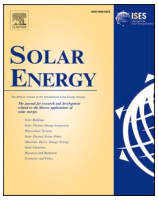

On optimum designs of linear Fresnel solar collectors

André Vitor Santos *, Diogo Canavarro, Pedro Horta, Manuel Collares-Pereira

University of Évora – Renewable Energies Chair, Polo da Mitra da Universidade de Évora, Edifício Ário Lobo de Azevedo, 7000-083 Nossa Senhora da Tourega, Portugal

ARTICLE INFO

Handling editor: .

Keywords:
Linear Fresnel collector
Optical analysis
Geometric optimization

ABSTRACT

This paper investigates the optimal design of linear Fresnel collectors using a two-objective optimization strategy aimed at maximizing annual energy efficiency while minimizing the specific direct cost of the solar field. The analysis then compares Pareto- optimal solutions for non-uniform designs (where geometric parameters such as width, shift, and radius vary) with solutions for variable radius configurations (constant width and shift). Additionally, the study evaluates whether the curvature radius can be effectively decoupled from other optimization parameters. The results in this paper show that non-uniform designs generally provide greater cost-effectiveness, particularly in certain regions of the objective space. While some areas show negligible differences between configurations, others distinctly favor non-uniform designs, although the differences are not significant and are reduced as the number of mirrors in the primary field increases. Furthermore, an analysis through dimensionless parameters highlights clear trends among the Pareto solutions. The investigation also reveals that predefined curvature radius criteria, such as the sun reference or Iparraguirre's model, yield outcomes nearly identical to optimization-based solutions for both uniform and non-uniform configurations. Consequently, curvature radius can be decoupled from other design parameters, significantly reducing computational complexity without compromising performance. The insights presented are valuable for advancing cost-effective designs of linear Fresnel collectors. Nevertheless, the conclusions rely on a simplified cost model, highlighting the need for more comprehensive cost modeling. However, developing such detailed models remains challenging due to limited operational data stemming from the low commercial maturity of linear Fresnel technology.

1. Introduction

The Linear Fresnel Collector (LFC) is a solar concentrator technology mainly used for thermal applications. It is composed of a primary field of reflectors slightly elevated from the ground whose purpose is to reflect (and concentrate) the incident sunlight on a fixed linear receiver located above the primaries [1,2]. Each mirror performs a single-axis tracking to follow the Sun's daily movement. The receiver has an absorber element to convert the reflected radiation to thermal energy, transferring it to a heat transfer fluid.

A geometric model of the LFC is illustrated in Fig. 1. The primary field has n mirrors, each one defined by three parameters: w_i, m_i, and κ_i – width, position, and curvature, respectively, with $i = \{1, 2, \cdots, n\}$. Moreover, s_i stands for the shift between two primaries, the distance between the center of neighboring mirrors, so that $s_i = m_i - m_{i+1}$. The gap, g, between mirrors stands for the empty space, meaning $g_i = s_i - (w_i + w_{i+1})/2$. Then, $W_p = [\mathbf{F}_1, \mathbf{F}_2]$ stands for the primary field width, given by the Euclidian distance between points $\mathbf{F}_1$ and $\mathbf{F}_2$, the edges of the primary field.

Usually, primary mirrors can be flat ($\kappa_i = 0$), parabolical (κ_i varies along the mirror width) or cylindrical (κ_i is constant). A previous work [3] shows that parabolic and cylindrical mirrors are indistinguishable from the receiver perspective for a fair range of design conditions. Thus, only cylindrical ones are hereafter considered since they are simpler to design and cheaper to manufacture. In this sense, the parameter κ_i is replaced by R_i, which stands for the curvature radius of the ith primary mirror, a more common geometric parameter. For convenience, flat mirrors are then defined by $R = 0$.

The model in Fig. 1 shows that the receiver is located at a height H_R above the primary field, a position that coincides with the center of the absorber, which in this case has a tubular shape. The receiver also comprises a secondary optics of aperture size given by W_s, displaced from the tube center a height h_s, and whose profile is defined by the shape function $z_s(x)$. At the secondary optic aperture midpoint is located the point $\mathbf{F}$, the aim-point of the primaries to perform the tracking procedure needed to follow the apparent movement of the sun.

In the context of Solar Thermal Electricity (STE), the linear Fresnel

* Corresponding author.
E-mail address: avas@uevora.pt (A.V. Santos).

https://doi.org/10.1016/j.solener.2025.113852
Received 15 April 2025; Received in revised form 6 July 2025; Accepted 31 July 2025
Available online 6 August 2025

Nomenclature

Latin characters

[**A**,**B**]	Euclidian distance between points **A** and **B**
A_{abs}	Absorber tube surface area [m^2]
A_{net}	Concentrator mirror (reflective) aperture area [m^2]
F	Primary mirrors tracking point. The aim (focus) at the receiver
$\mathbf{F}_1, \mathbf{F}_2$	Primary field edge points
g	Gap between two neighboring mirrors [m]
h_s	Height difference between absorber and secondary optic aperture [m]
H_R	Receiver height [m]
I_{min}	Flux intensity threshold at the absorber [W/m^2]
m	Horizontal (x-axis) position of a primary mirror [m]
M	Center point of a primary mirror.
n	Number of mirrors in a primary field [-]
N_{pop}	Number of individuals in a population [-]
r_a	Evacuated tube absorber radius [m]
r_{go}	Evacuated tube glass cover outer radius [m]
r_{gi}	Evacuated tube glass cover inner radius [m]
R	Curvature radius of a primary mirror [m]
s	Shift (distance between center points) between two neighboring mirrors [m]
w	Primary mirror width [m]
W_p	Primary field width [m]
W_s	Secondary optic aperture width [m]
$\widehat{x}$	Decision vector

Greek characters

Γ	Direct specific cost of a linear Fresnel solar field [€/m^2]
θ_L	Longitudinal incidence angle [°]
θ_{LS}	Longitudinal-solar incidence angle [°]
θ_T	Transversal incidence angle [°]
κ	Curvature profile of a primary mirror
σ_{mu}	Standard deviation of the (zero mean) Gaussian mutation operator
π_1	Filling factor of a linear Fresnel configuration: $\pi_1 = \sum w_i / W_p$
π_2	Shape factor of a linear Fresnel configuration: $\pi_2 = W_p / 2H_R$
π_3	Pitch factor of a linear Fresnel configuration: $\pi_3 = s/w$

Abbreviations

CAPEX	Capital Expenditures
CEC	Compound Elliptical Concentrator
DEAP	Distributed Evolutionary Algorithm in Python
ECF	Energy Collection Factor [-]
EW	East-West
LFC	Linear Fresnel Collector
NS	North-South
NSGA-II	Elitist Non-dominated Sorted Genetic Algorithm
OPEX	Operational Expenditures

Indexes

h	Hour index
i	General counting index for the mirrors in a primary field
k	General counting index

technology is having difficulties reaching a state of maturity. In part because of its lower optical efficiency when compared to competing technologies, such as parabolic troughs and central receiver systems [4–8]. The lower efficiency is mainly caused by geometrical characteristics that affect its optical performance. For this reason, related studies deal with geometric designs to find a way around such efficiency problems. On the one hand, optical losses are well-known: cosine effect, shading, blocking, spillage, and end-losses [9]. On the other hand, the number of geometric variables that can be manipulated is large, and the concentrator simplicity imposes a few restrictions to the design of solutions. Indeed, the literature regarding the linear Fresnel collector design is vast, although diffuse in approaches, methods, and results.

Solutions developed to enhance the optical performance include the proposition of new conceptions of concentration such as the compact design [9], the etendue-match approach [10], the use of catoptric primaries [11], a tilted primary field [12,13], simultaneous multiple surfaces design [14], dual asymmetric receiver [15], beam-down design [16], and, more recently, an aplanatic approach [17]. Although

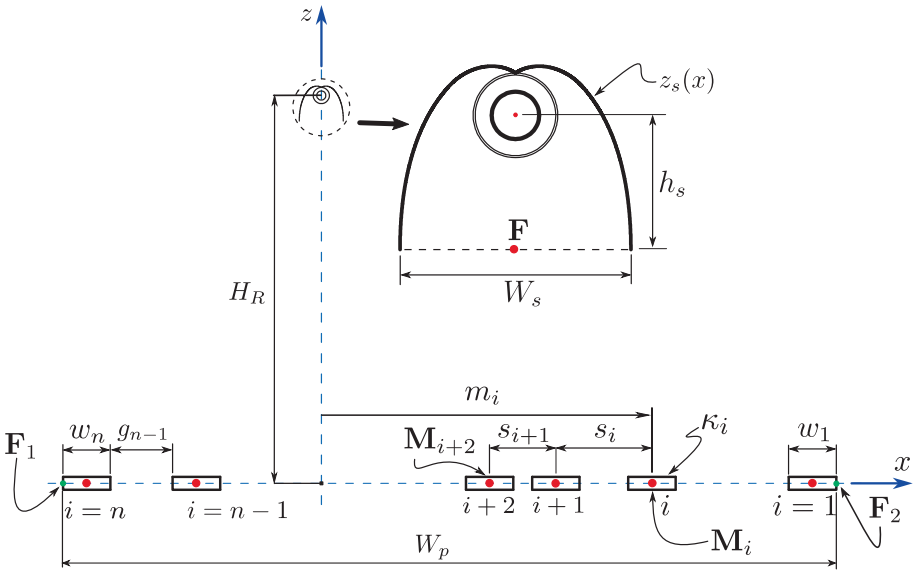

Fig. 1. A geometric model of the Linear Fresnel Collector (LFC). The figure illustrates the main parameters in an LFC concentrator and exemplifies the case of a receiver composed of a Compound Elliptical Concentrator (CEC) secondary optic and an evacuated absorber tube.

presenting promising results, disadvantages also arise such as the addition of more geometric parameters, so that optimum designs for each one of these new conceptions are new problems. In this work, only the standard LFC shown in Fig. 1 is considered to show the related gains, even though the concepts developed could equally well be used together with the refereed alternative solutions.

In short, the literature concerning the standard linear Fresnel collector comprises studies analyzing particular optical losses to propose design criteria on how to calculate some decision variables [18–24]. It also comprises studies that take the approach of an optimization problem [25–31], where decision variables, constraints, and objective functions are defined, and then parametric analysis [31], gradient-based methods [25] or computational intelligence tools [26–30] are used as search heuristics to determine optimum set of variables.

In general, results from these works are not in accordance, and the comparison is not easy: the dimensions (sizing) vary due to different applications and constraints. They comprise different primary field configurations; single [25,27,28] and multi-objective [26,30] approaches defined by a wide range of objective functions based on different metrics [23,26–28] and cost models [22,25,26]; performance computations comprise instantaneous [29], daily [26,28,32], and annual [22,23,25,27,30,31] analyses.

Nevertheless, some dimensionless parameters can be defined to be used as a comparison basis and, thus, different works can be confronted. One parameter is the filling factor, $\pi_1 = \Sigma w_i / W_p$, which stands for a packing measure of the primary field – higher filling factors means denser fields. Another is the shape factor, π_2, here defined as $\pi_2 = W_p / 2H_R$, used to represent an overall proportionality metric width and height of the concentrator. The last, π_3, is the pitch factor, defined by the pitch-to-width ratio, so that $\pi_3 = s/w$.

A summary of reported optimum parameters is presented in Table 1. This selection includes studies that provide enough design data to calculate the dimensionless parameters but does not represent an exhaustive review of the literature. As shown, the reported parameters vary significantly across the different studies. This variability can reasonably be attributed to differences in geographic location and collector orientation [30,31], which influence the distribution of solar incidence angles and the availability of sunlight. Additionally, distinct optimization objectives – such as maximizing optical efficiency, minimizing land use, or reducing costs – contribute to variations in the resulting geometries, as noted by Montes et al. [23]. While the literature cannot support broad generalizations, it does offer valuable insights.

The majority of studies deal with uniform primary fields (all mirrors have the same width and curvature radius, and are evenly spaced) [27,28,30–33]. Normally, studies that tackle non-uniform configurations does it by an analytical pre-design [19–21] in which some variables are calculated based on design criteria and only few of them are treated as decision variables to be optimized by the search heuristic – a strategy to reduce the number of variables and simplify the problem.

Evidence suggest that primary field with non-uniform configurations of width and shift do not significantly increase energy collection [19–21,25]. Some results [19–21] are based on an analytical pre-design, which constrains the search space and might lead to local optima (biased) results. Another [25] used the cost-energy ratio as the objective function to be minimized, transforming a two-objective problem (cost and efficiency) into a single objective one – a strategy that can lead to only a single Pareto solution and difficulties a more general assessment. On the one hand, it is strikingly that different studies through different approaches have found that these non-uniform designs do not have a significant impact on performance in comparison to the uniform design. On the other hand, most of these studies do not include an economic model and only consider energy collection [19–21]. Another previous work [24] verified that the collected energy per unit of reflective area was lower for their non-uniform shift proposition. Only Boito and Grena [25] have included a cost model, but a rather simple and linear one. Thus, a reasonable research question to be further investigated rises:

- are non-uniform designs of width and shift more cost-effective than variable-radius designs (with constant width and shift)?

Regarding the curvature radius design of the primary mirrors, the different studies concerning the optimal radius [18–21,34,35] holds a fundamental underlying hypothesis that, of course, might not be true and should be verified: they assume the curvature radius as a decoupled variable that can be optimized in a step after other geometric parameters (such as mirrors widths and pitches, receiver height, among others) – only Boito and Grena [25] include the curvature radius in the optimization routine with the other decision variable – their results indicate that different configurations of curvature radius (uniform or non-uniform) have a meager impact on the other geometric parameters. Then, the following research question is established:

- can the curvature radius be decoupled from other decision variables in design optimization?

In line with this strategy, instead of identifying a single optimal

Table 1
Dimensionless parameters reported regarding linear Fresnel collector optimal designs. The listed studies represent a non-exhaustive selection of relevant proposals in the literature. Selection was mainly based on the availability of data to calculate dimensionless parameters.[1]

Reference	Location	Orientation	Configuration	$\Sigma w_i / W_p$	$W_p / 2H_R$	s/w
Nixon and Davies [22]	E72.65°, N23.22°	NS	C-W & V-S & C-R	0.647	0.865	var
Montes et al. [23]	E2.36°, N37.11°	NS	C-W & C-S & V-R	0.720	1.000	1.405
Sharma et al. [31]	E76.95°, N8.48°	NS	C-W & C-S & C-R	0.616	1.160	1.65
		EW		0.826	0.865	1.22
	E72.63°, N23.07°	NS		0.581	1.229	1.75
		EW		0.728	0.982	1.39
	W1.6°, N38.27°	NS		0.548	1.305	1.86
		EW		0.623	1.147	1.63
Boito and Grena [25]	Not reported	NS	C-W & C-S & C-R	0.832	1.502	1.21
			C-W & V-S & C-R	0.836	1.497	var
			C-W & C-S & V-R	0.828	1.603	1.127
			V-W & V-S & V-R	0.829	1.661	var
Moghimi et al. [26]	Do not Apply	Do not Apply	C-W & C-S & V-R	0.968	0.718	1.034
Cheng et al. [27]	E115.90°, N23.45°	EW	C-W & C-S & C-R	0.510	0.649	2.000
Ajdad et al. [28]	W8.0°, N31.62°	NS	C-W & C-S & C-R	0.786	0.639	1.297
Ahmadpour et al. [32]	E48°18′, N38°12′	Not reported	C-W & C-S & C-R	CBC	CBC	CBC
López-Núñez et al. [29]	W99.23°, N18.54°	Not reported	C-W & V-S & C-R	CBC	CBC	var

[1]In the "Configuration" column, C and V refer to constant and variable geometric settings, respectively, and W, S, and R refer to width, shift, and radius of primary mirrors, respectively – thus, C-W stands for constant width, while V-R stands for variable radius. In the "Orientation" column, NS and EW refer to North-South and East-West, respectively. CBC refers to parameters that cannot be calculated due to missing data in the original paper.

solution, this work aims a theoretical exploration to provide additional insights into the generalization of the design problem. The primary goal is to deepen the understanding of the more subtle aspects of this problem by introducing meaningful simplifications that reduce it to its most essential form or at least clarify how a simplified design affects optical performance.

To address these questions, this study adopts a multi-objective optimization approach, focusing on energy efficiency and cost, as optical, thermal, and economic factors are essential for evaluating overall performance. This approach enables a comprehensive assessment of different geometric configurations through the analysis of trade-offs between the objectives, as reflected in the resulting Pareto solutions. Accordingly, the structure of this work is as follows. Section 2 outlines the methodology, defining decision variables, performance models, and objective functions that link a specific geometric configuration to key metrics, such as annual useful energy efficiency and the direct specific cost of the linear Fresnel collector. Finally, this section introduces an evolutionary algorithm used to solve the global optimization problem. Section 3 presents the optimization results and discusses each of the previously defined research questions. Lastly, Section 4 presents the conclusions and suggests directions for future research.

2. Materials and methods

2.1. Overview and decision variables

Fig. 1 presents a geometric model for the standard Linear Fresnel Collector (LFC). Among all geometric parameters some are considered as decision variables to be optimized, while others are defined by constraints of the problem.

The context of solar thermal electricity application refers to high-temperature heat generation (>400 °C) [36,37], and the use evacuated tubes [38] is a practical constrain due to its low thermal losses under such conditions [39,40]. Commercial availability imposes a restriction on the size of these tubes, and, here, the 70 mm diameter evacuated tube [38] is defined as the absorber element – the smallest option, which leads to higher concentration and lower thermal losses. The geometric characteristic of this tube are presented in Table 2: r_a refers to the absorber tube radius, while r_{go} and r_{gi} stands for the outer and inner glass cover radius, respectively.

The receiver in Fig. 1 comprises a secondary optic. Here, an edge-ray CEC (Compound Elliptical Concentrator) is considered as the secondary. It has the lowest possible gap between the optic and the absorber – that is, the cusp point touches the outer glass cover of the absorber tube. This CEC geometry is a consequence of the other parameters and does not add new parameters to the model shown in Fig. 1. Moreover, this edge-ray CEC design yields a secondary optic that simultaneously maximizes efficiency, flux uniformity, and tolerance to optical errors [41]. Thus, the aim of this study concerns mainly the primary field and receiver position. A detailed explanation of the CEC edge-ray design can be found in other publications [41,42].

By considering these constraints regarding the receiver, the design of a linear Fresnel collector relates to the definition of the following geometric parameters: width, position, and curvature radius (w, m, and R, respectively) of the n primary mirrors, and the receiver height (H_R). In this sense, a non-uniform configuration is defined by the following decision vector: $\hat{x} = \{n, \{w_1, m_1, R_1\}, \cdots, \{w_n, m_n, R_n\}, H_R\}$, which involves $3n + 2$ decision variables. A uniform configuration is defined by $\hat{x} = \{n, w, s, R, H_R\}$, which has only five decision variables. Of course, it is also possible to consider uniform and non-uniform settings for only particular parameters such as w and R, for example. Moreover, a symmetric design also leads to a significant reduction in the number of geometric parameters to be defined.

Table 2
Evacuated tube geometric characteristics [38]. r_a refers to the absorber tube radius, while r_{go} and r_{gi} stands for the outer and inner glass cover radius, respectively.

r_a [m]	r_{go} [m]	r_{gi} [m]
0.035	0.0625	0.0595

2.2. Performance models

The performance of a linear Fresnel collector can be evaluated under three aspects. One is the optical component, which represents the energetic input on the system. The thermal aspect evaluate the production of useful heat by assessing the thermal losses, while the economical aspect gives a metric of the cost of produced energy. Here, the power block computations that account for the heat-to-electricity conversion are not considered because it would be a common factor among all different configurations.

Energy efficiency computations must consider an annual time frame to account for all incident solar irradiation at a particular location. To reduce the total computation time of ray-tracing simulations other authors have define surrogate models for an annual analysis: Abbas and Martínez-Val [21] compute only twelve representative days (the 21st of each month); Cheng et al. [27] and Men et al. [30] have considered four representative days (solstices and equinoxes); others simply consider a daily average [26,28,32] or just instantaneous values [29]. In this work, an actual annual analysis is carried out.

2.2.1. Energy efficiency model

Here, the useful energy efficiency is calculated by a steady-state model that accounts for the absorbed energy (optical input) above a threshold of flux intensity on the absorber (heat losses). This analysis is based on hourly averages to compute the annual yield.

To this end, the optical performance of each configuration is computed by an analytical method [43], avoiding time-consuming ray-tracing simulations. The method determines the flux at a flat receiver, representing the aperture of the secondary optic. For each configuration, defined by a decision vector $\hat{x}$, an edge-ray CEC secondary is designed, and the flux at its aperture, a flat target of width W_s located h_s below the tube center, is computed. Moreover, the aim-point of the primary mirrors for the tracking procedure is the mid-point of this flat target. While W_s and h_s vary across configurations, the CEC is consistently designed using the edge-ray technique, ensuring a tailored secondary optic for each case.

Additional optical losses occur after the concentrated flux enters the secondary optic aperture. These include reflections at the secondary surface, transmission losses through the glass cover, and the absorptivity of the absorber tube. Moreover, some rays may undergo multiple reflections and transmissions or may exit the receiver without being absorbed. All of these effects are collectively represented by the “optical efficiency of the receiver”, defined as the ratio of absorbed flux to the flux entering the secondary aperture.

The methodology assumes that this optical efficiency remains approximately constant despite changes in transversal and longitudinal incidence angles, and across different edge-ray CECs. These assumptions are based on the idea that the receiver’s optical efficiency primarily depends on fixed characteristics of the system – namely, the secondary optic reflectivity, glass cover transmissivity, and absorber absorptivity – which remain unchanged across all configurations evaluated in this comparative study.

Thus, it is assumed that the receiver (comprising the edge-ray CEC and evacuated tube) does not contribute to differences in useful efficiency between configurations, and that the flux at the aperture is sufficient to identify the configuration with the higher yield.

This optical model computes the efficiency for a particular incidence direction based on transversal and longitudinal incidence angles, θ_T and

θ_L, respectively. The optical characterization determines the optical efficiency for an incidence range in which $\theta_L \in [0^\circ, 85^\circ]$ and $\theta_T \in [-85^\circ, 85^\circ]$ for asymmetric primary fields or $\theta_T \in [0, 85^\circ]$ for symmetric primary fields. At θ_L or θ_T equals to 90°, the efficiency is set to zero. The annual analysis is based on hourly data of a typical meteorological year taken from the PVGIS application program interface [44]. For each of the 8760 h of the year, sun azimuth and zenith are calculated by a solar position algorithm [45] and then converted to transversal and longitudinal incidence angles, θ_T and θ_L, respectively.

In this work, the Energy Collection Factor (ECF), as shown in Eq. (1), is the metric used to represent the amount of useful energy efficiency produced by a particular geometric configuration, in the meaning that $\mathrm{ECF} = \mathrm{ECF}(\hat{x})$.

$$\mathrm{ECF} = \frac{\sum_{h=1}^{8760} \left[\eta_T(\theta_T^h)\cdot\eta_L(\theta_{LS}^h)\cdot I_b^h \cdot A_{net} - I_{min}\cdot A_{abs}\right]^+}{\eta_0 \sum_{h=1}^{8760} I_b^h \cdot A_{net}} \tag{1}$$

In Eq. (1), the optical efficiency for a particular incidence direction is computed by the factorized approach [46], and a better approximation is achieved by using the longitudinal-solar incidence θ_{LS} [47,48]. The terms η_T and η_L stands for the transversal and longitudinal optical efficiencies of this factorized approach, respectively, while η_0 is the optical efficiency at normal incidence. Moreover, this analysis considers conditions of sunshape and optical errors of state-of-the-art mirror panels [19], as shown in Table 3.

In the yield model shown in Eq. (1), the thermal losses are included by I_{min} and the positive sign (+). The first represents a threshold of flux intensity, which together with the latter means that only the flux at the absorber above a particular threshold is computed as useful heat. The terms A_{net} and A_{abs} represent mirror and absorber areas of the linear Fresnel configuration. Furthermore, I_b stands for the direct normal (or beam) irradiance, and h is an index that ranges for each of the 8760 h of the year.

Abbas et al. [20] argues for $I_{min} = 25.0\ \mathrm{kW/m^2}$ to reach temperatures higher than 400 °C, but this data comes from studies that account for non-evacuated receivers, which implies considerable higher thermal losses. For an evacuated receiver operating at temperatures of 560 °C, modelling and experimental works [39,49,50] indicate thermal losses per unit of absorber surface up to 5.0 $\mathrm{kW/m^2}$ for a 70 mm diameter absorber tube. Thus, this work considers $I_{min} = 5.0\ \mathrm{kW/m^2}$ – the absorber flux intensity threshold necessary to overcome thermal losses and produce useful heat.

2.2.2. Cost model

A geometric cost model relates parameters shown in Fig. 1 to a metric of the direct specific cost of the linear Fresnel concentrator, Γ, given in units of €/$\mathrm{m^2}$ of mirror aperture area. Therefore, Γ is a function of the geometric settings, and one can write $\Gamma = \Gamma(\hat{x})$.

The functional relationship used in this work for Γ follows the equations proposed by Mertins [51], but in a more generalized formulation to include variations of the decision vector other than the simple uniform configuration. Mertins' model was also used in the work carried out by Moghimi et al. [26] but with a modification to account for a multi-tube receiver.

Here, Γ is given by Eq. (2), where c_m, c_g, c_e, and c_r refers to mirror, gap, elevation, and receiver cost factors, respectively. Moreover, w and g stands for the width and gap of a primary mirror, respectively, H_R is the receiver height, and i is an index used to range for all n mirrors in the primary field.

$$\Gamma = \frac{1}{\sum_{i=1}^{n} w_i}\left[\sum_{i=1}^{n} c_{m,i} + \sum_{i=1}^{n-1} c_{g,i}\cdot g_i + c_e\cdot(H_R + 4.0) + c_r\right] \tag{2}$$

To develop the cost factors that comprise Γ, Mertins [51] used empirical data from the SOLARMUNDO project, scale relationships, and logarithmic averages to project values of c_m, c_g, c_e, and c_r at a target size.

The mirror cost factor, c_m, represents the cost of the mirror per unit of length, and accounts for the reflective material, driving motors, tracking system, controllers, assembly, etc. Then, for a mirror width w, the corresponding mirror cost factor c_m is calculated as shown in Eq. (3), where w_0 and c_{m0} are the reference size and cost, respectively, and f_m is the scale factor, as given in Table 4.

$$c_m = c_{m0}\left(\frac{w}{w_0}\right)^{f_m} \tag{3}$$

The gap cost factor, c_g, represents the cost of the distance between two mirrors per unit of length. It relates to the distance between two neighbor mirrors when they are in a horizontal position. It is reasonable to assume that a higher gap increases cost as its uses more structuring material. For a gap g, the cost factor c_g is determined by Eq. (4), where g_0 and c_{g0} are the reference size and cost, respectively, and f_g is the corresponding scale factor, as shown in Table 4.

$$c_g = c_{g0}\left(\frac{g}{g_0}\right)^{f_g} \tag{4}$$

The elevation cost factor, c_e, relates with the receiver mounting at a height H_R. It is given per unit of length and unit of elevation, thus in €/$\mathrm{m^2}$. It follows a similar approach than in the cases of c_m and c_g, but based on the absorber tube diameter, d_a, and a variable scale factor, f_e, also a function of d_a, as in shown in Eq. (5). The reference size and elevation cost factor reported by Mertins [51] were for a tube diameter of 0.219 and a cost of 19.8 €/$\mathrm{m^2}$, respectively.

$$c_e = 19.8\ €/\mathrm{m^2}\left(\frac{d_a}{0.219\ \mathrm{m}}\right)^{f_e(d_a)} \tag{5}$$

f_e is calculated as given by Eq. (6), a logarithmic average of the three elevation subsystems shown in Table 5, where k is an index to range for all these subsystems.

$$f_e = \frac{\ln\left[\sum_k \left(\frac{c_{e,k}}{19.8\ €/\mathrm{m^2}}\right)\left(\frac{d_a}{0.219\ \mathrm{m}}\right)^{f_{e,k}}\right]}{\ln\left(\frac{d_a}{0.219\ \mathrm{m}}\right)} \tag{6}$$

The receiver cost factor, c_r, relates with the absorber tube, coatings, welding and construction, assembly and transportation. It is given per unit of length, thus in €/m. As in the case of c_e, it considers d_a as the scaling parameter and also a variable scale factor, as shown in Eq. (7). The reference size and receiver cost factor reported by Mertins [51] were for a tube diameter of 0.219 and a cost of 654.0 €/m, respectively.

$$c_r = 654.0\ €/\mathrm{m}\left(\frac{d_a}{0.219\ \mathrm{m}}\right)^{f_r(d_a)} \tag{7}$$

f_r is calculated as given by Eq. (8), a logarithmic average of the six

Table 3
Models of sunshape and optical errors considered for the optical analysis of a linear Fresnel geometric configuration.

	Sunshape	Optical errors
Profile	Pillbox	Gaussian
Size	4.65 mrad	5.0 mrad

Table 4
Mirror and gap cost factors for the SOLAMUNDO linear Fresnel collector [51].

c_{m0}	30.5 €/m	c_{g0}	11.5 €/$\mathrm{m^2}$
w_0	0.5 m	g_0	0.01 m
f_m	1	f_g	1

Table 5
Reference costs and scaling factors of elevation subsystems [51].

Elevation subsystem	$f_{e,k}$	$c_{e,k}$[€/m^2]
Construction	1.4	14.2
Transportation and packing	1	0.9
Assembly	1	4.6

receiver subsystems shown in Table 6, where k is an index to range for all these subsystems.

$$f_r = \frac{\ln\left[\sum_k \left(\frac{c_{r,k}}{654.0\ €/\mathrm{m}}\right)\left(\frac{d_a}{0.219\ \mathrm{m}}\right)^{f_{r,k}}\right]}{\ln\left(\frac{d_a}{0.219\ \mathrm{m}}\right)} \tag{8}$$

For this work, the mathematical models from Eqs. (2)-(8) were implemented in Python and yield the exact same cost as reported by Mertins [51] for a reference case: 99.2 €/m^2.

Here, it is important to highlight some aspects regarding this cost model. Γ is a metric of the solar field specific direct cost, a component of the engineering procurement and construction costs. Thus, it does not include other factors such as land, site preparation, storage, power block, among others that sums up the power plant Capital Expenditures (CAPEX) [52]. The influence of the curvature radius (values and non-uniform configurations) on Γ is not included. On the one hand, usually $R \gg w$ and mirrors are almost flat, leading to negligible additional cost due to the use of more reflective material (which occurs in parabolic trough collectors). On the other hand, some additional steps in the manufacturing process of bent mirrors [53] can indeed lead to increase in costs. Moreover, non-uniform configurations regarding w and R can have an influence on the Operational Expenditures (OPEX) due to the need for more spare parts, which are not included here. In this sense, the presented cost model assumes negligible effects on OPEX, an assumption that might not be true. However, further analysis of how non-uniform configurations affect CAPEX and OPEX lies beyond the scope of this work.

It should be noted that Γ does not represent the energy cost of a solar plant as typically defined by the Levelized Cost of Electricity (LCOE). An LCOE-based analysis would require consideration of additional factors beyond the definition of an optimal geometric configuration and the corresponding solar field specific direct cost, including plant sizing, thermal storage, balance of plant, power block performance, and comprehensive annual electricity production and cost assessments (CAPEX and OPEX) of the whole plant [52]. Such an analysis lies beyond the scope of this work.

Lastly, the reported values are from 2009 and should be corrected by inflation. However, from a comparison point-of-view, the functional relationships within the model are more important than the current monetary values. For this reason, the base values of this model were not corrected up to today's inflation.

2.3. Optimization approach

2.3.1. Problem definition

Considering the performance metrics presented in Section 2.2, the aim is to find a decision vector which simultaneously yields the highest ECF and lowest Γ; that is, the objectives are to find maximum efficiency and minimum cost. This optimization problem is defined in Eq. (9), where ECF and Γ are the objective functions that relates the performance of a geometric configuration defined by the decision vector $\hat{x}$.

$$\begin{cases} \max \mathrm{ECF}(\hat{x}) \\ \min \Gamma(\hat{x}) \end{cases} \tag{9}$$

A general decision vector $\hat{x} = \{n, \{w_1, m_1, R_1\}, \cdots, \{w_n, m_n, R_n\}, H_R\}$ corresponds to a full non-uniform configuration and its size is a function of n, the number of mirrors comprising the primary field. Usually in the literature [19,20,25,27,30,33], n is fixed and the other parameters are decision variables to be optimized by the search heuristic since find the optimum $\hat{x}$ with changing number of decision variables is a quite hard task. Here, two sizes of primary fields are addressed: $n = 12$ and $n = 25$.

As reported by many works [8,20,21,31], the East-West (EW) orientation have a lower annual efficiency than the North-South (NS) case. For this reason, only the NS orientation is considered in this work, and geometric configurations are assumed to be symmetric, so that, for example, $\{w_1, m_1, R_1\} = \{w_n, -m_n, R_n\}$. Moreover, it is easier to work with the gap, g, as a decision variable instead of mirror position or shift (m or s), as it makes unnecessary to account for feasible solutions that must obey a shift large enough for two neighboring mirrors to not collide. Then, $\hat{x}$ is a function of w, g, R, and H_R, where these variables are subjected to bounds as given by Table 7.

For this matter, different configurations of primary field must be defined in order to address the research questions established in Section 1 (*Introduction*). First, the NUN case refers to a full non-uniform setting, where each mirror has particular values of w, g, and R, and all of them are subjected to the optimization routine. The VAR refers to the case of a primary field in which mirrors have constant values of width and gap (w and g) but with a variable radius (R), and all of them are subjected to the optimization routine. The NUN-sunRef is denominated by a non-uniform configuration in which w and g are subjected to optimization but R is calculated as given by the sun reference criteria [19]. UN defines a full uniform configuration, a geometric setting in which the primary field is defined by constant values of w, g, and R, all of them are subjected to the optimization routine. The UN-IpaRef stands for a configuration in which the primaries have constant values of w, g, and R, but only the first two are subjected to the optimization routine, while R is calculated by the criteria proposed by Pulido-Iparraguirre et al. [54].

Moreover, computations for ECF vary depending on a selected location since the annual distribution of beam irradiance and incidence angles change from one place to another. In this work, Evora (Portugal) is considered for the calculations, though it can be replicable to any other location. Evora general data is presented in Table 8.

2.3.2. Search algorithm

The problem defined in Eq. (9) relates to an unconstrained multi-objective optimization [55,56]. Both ECF and Γ must be simultaneously optimized, and instead of a single optimum decision vector, $\hat{x}^*$, a set of optimal solutions, $\{\hat{x}_1^*, \cdots, \hat{x}_N^*\}$, the so-called Pareto solutions, should be determined to represent the trade-off between objectives. In this context, evolutionary algorithms, as are stochastic population-based methods, are a proven strategy to determine the Pareto front of optimum solutions [57].

In this work, the evolutionary algorithm starts by generating a random population of N_{pop} individuals – each individual is a candidate

Table 6
Reference costs and scaling factors of receiver subsystems [51].

Receiver subsystem	$f_{r,k}$	$c_{r,k}$[€/m]
Absorber tube	2	116.2
Selective coating	0.9	56.6
Welding	0.7	116.4
Construction	1.4	136.5
Transportation and packing	0.6	26.4
Assembly	0.6	112.6

Table 7
Decision variables bounds for the optimization search.

H_R[m]	w[m]	g[m]	R[m]
[4.0, 20.0]	[0.2, 2.0]	[0, 2.0]	[0, 100.0]

Table 8
Location data used for energy efficiency analysis, based on typical meteorological year data (2006–2016) from PVGIS. Solar angles are computed hourly for Évora, Portugal.

Location	Latitude	Longitude	$\sum_h I_b^h$
Evora (Portugal)	38.53°	−8.0°	2229.2 kWh·m^{-2}·year^{-1}

solution defined by a decision vector. This population is evaluated and the corresponding fitnesses are defined by the objective functions (ECF and Γ). An offspring of N_{pop} individuals (children) is produced from the population by parents (mate) selection, followed by crossover and mutation. From the poll of individuals given by the union of population and offspring (size $2N_{pop}$), N_{pop} individuals are selected (survivors selection) to form a new population, to then produce a new offspring and so on [58,59]. This cycle repeats itself until a stopping criterion is satisfied, and the Pareto solutions are then sorted from the final population. A flow diagram of this evolutionary process is presented in Fig. 2.

This evolutionary search heuristic was implemented based on the DEAP (Distributed Evolutionary Algorithm in Python) framework [60]. An individual (candidate solution) is coded as a list of real numbers between 0 and 1 (genes) and is decoded to the decision variable space (subjected to the bounds shown Table 7) to fitness evaluation. The selection mechanisms are based on dominance and crowding distance following the elitist Non-dominated Sorted Genetic Algorithm (NSGA-II) [61].

A solution B dominates another solution C if B is not worse than C in all objectives and B is strictly better than C in at least one objective. If neither B dominates C nor C dominates B, they are considered non-dominated. NSGA-II sorts the population into non-dominated fronts to rank solutions. The first non-dominated front consists of solutions that are not dominated by any other solution in the population – these are given rank 1. The second front (rank 2) holds individuals that are only dominated by those in the first front, and subsequent fronts contain solutions that are dominated by previous ones. The crowding-distance is a metric used to maintain diversity in the population by estimating the density of solutions surrounding a particular individual. It quantifies how close a solution is (in the objective space) to its neighbors within a non-dominated front. Therefore, high crowding distance means that a solution is in a sparse region (likely to be selected), while low crowding distance means that the solution is in a dense region (less chance of being selected).

Parents selection considers a tournament of two individuals randomly selected from the population. First, they are compared based on dominance – wins the individual which dominates the other, i.e., the one with the lowest rank. If they are non-dominated, wins the individual with higher crowding distance. Survivor selection is based on a combination of non-dominated sorting and crowding distance to ensure both convergence and diversity. First, individuals in the pool (population and offspring) are ranked into non-dominated fronts, where solutions in lower-ranked fronts (better Pareto-optimal solutions) are prioritized for selection. If the number of individuals in selected fronts exceeds the population size, the last front is sorted based on crowding distance, which measures how isolated a solution is in objective space. Solutions with higher crowding distance are preferred to maintain diversity. This ensures that the next generation retains high-quality and well-distributed solutions along the Pareto front.

Due to the computational cost of ECF evaluations, $N_{pop} = 200$ and the stopping criteria is a number of 400 (four hundred) generations, divided into two steps of 200 generations, each one with different settings of the same evolutionary operators: two-point crossover and (zero mean) Gaussian mutation. As shown in Table 9, there are probabilities for both crossover and mutation to take place, and σ_{mu} refers to the standard deviation of the Gaussian mutation operator. The first 200 generations runs with the evolutionary operator eoA, while the last 200 generations runs with eoB.

Further details about NSGA-II can be found in the works by Deb [57] and Eiben and Smith [59], while DEAP documentation has more

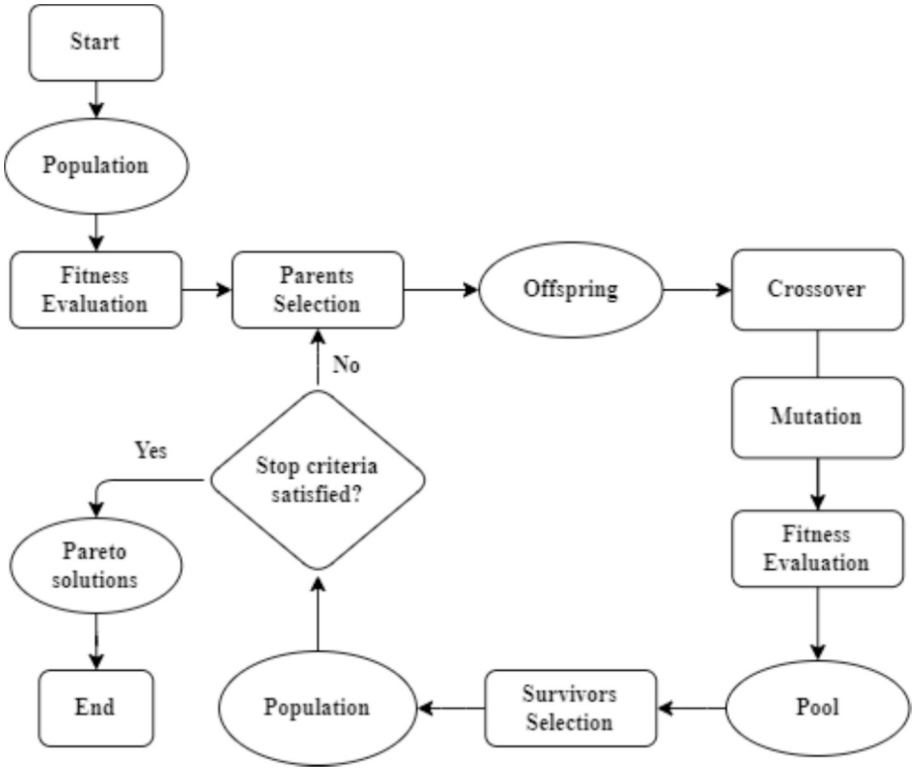

Fig. 2. Flowchart of the evolutionary optimization process. A population of candidate solutions is iteratively evolved through selection, crossover, and mutation. Fitness is evaluated at each step, and survivors form the next generation. The process repeats until stopping criteria are met, yielding Pareto-optimal solutions.

Table 9
Evolutionary operators used across two 200-generation phases: eoA (first half) and eoB (second half). Parameters include crossover and mutation probabilities, and σ_{mu}, the standard deviation of the Gaussian mutation.

Evolutionary Operators	Crossover probability	Mutation probability	σ_{mu}
eoA	0.8	0.40	0.2
eoB	0.5	0.25	0.1

information on the evolutionary operators.

3. Results and discussion

3.1. Non-uniform configurations analysis

Results from previous works [19–21,25] highlighted that the non-uniform configuration might not be cost-effective, as it yields a slightly higher efficiency than a variable radius design but may imply more costs, which leads to a reasonable question: is the non-uniform design (NUN) more cost-effective than the variable radius (VAR) case? To this end, this section presents a comparison of NUN and VAR optimum geometries.

Fig. 3 shows a comparison of optimal solutions for optimization problem defined in Section 2.3.1, considering cases where the primary field is composed of (a) $n = 12$ and (b) $n = 25$ mirrors. As seen, the Pareto fronts clearly show a trade-off between efficiency (ECF) and cost (Γ) – as efficiency increases, costs rise significantly, showing an asymptotic behavior in all cases. The red dashed lines indicate the maximum efficiency, ECF^{max}, and minimum cost, Γ^{min}, achieved within each case. Therefore, many solutions have quite the same cost but with slightly increasing efficiencies; other solutions have practically the same efficiency but with highly increasing costs; then, there are solutions presenting a smoother trade-off between these asymptotic cases.

In general, Fig. 3 shows that NUN (blue points) and VAR (orange points) configurations have similar trends. Previous works [19–21,25] have found a meager difference between non-uniform and variable radius designs, as it is shown in Fig. 3 for a wide region of the objective space. However, this figure also shows that in a region, for a particular value of efficiency, non-uniform designs have a lower cost than variable radius designs (or a higher efficiency for a reference cost). Moreover, these results indicate that the difference between non-uniform and variable radius is more noticeable for a primary field with fewer mirrors, and as the number of mirrors increases, the benefit of the fully non-uniform design diminishes.

In short, results in Fig. 3 indicate that non-uniform designs are more cost-effective solutions, however, the performance difference is reduced as the number of mirrors in the primary field increases. In the theoretical limit case of a large number ($n \to \infty$) of tiny mirrors ($w \to dw$), there would be no differences between these configurations.

Fig. 4 provides a geometric perspective of the Pareto solutions in Fig. 3 by plotting two dimensionless parameters: filling factor, $\pi_1 = \Sigma w_i / W_p$, and shape factor, $\pi_2 = W_p / 2H_R$. Each point corresponds to a different geometric configuration, meaning that a direct comparison between solutions is complex, especially for non-uniform designs where mirror parameters vary individually. Despite this complexity, the scatter plots reveal two clear trends that apply to both configurations: a set of trivial solutions where π_1 is approximately 1, and a more structured trend for the remaining data points.

The trivial solutions, where $\pi_1 \approx 1$, result from primary fields with minimal spacing between mirrors ($g \approx 0$). In these cases, π_2 varies significantly, reaching extreme values, particularly in the variable radius configuration. When disregarding these high π_1 cases, a second trend emerges, showing that the shape factor tends to remain below an upper bound, specifically $\pi_2 < 1$. Additionally, the results indicate that for comparable π_1 values, the variable radius design generally exhibits higher π_1 values than the non-uniform cases. This suggests that while allowing radius variation provides flexibility, it also leads to larger primary field width relative to receiver height, which could introduce practical design constraints.

To understand how dimensionless parameters influence the Pareto solutions, Fig. 5 presents scatter plots relating efficiency (ECF) and cost (Γ) to geometric characteristics for the case $n = 12$. As observed in Fig. 5a and Fig. 5d, efficiency and cost generally decrease as π_1 increases. However, when π_1 approaches 1, Γ stabilizes while ECF continues to decline. This trend reflects the behavior observed in Fig. 3a, where these trivial solutions ($g \approx 0$) lead to an asymptotic horizontal limit. The trivial cases for variable radius configurations correspond to a pitch factor, $\pi_3 = s/w$, so that $\pi_3 = 1$, as shown in Fig. 5c and Fig. 5f. Additionally, as s/w increases, both ECF and Γ increase, indicating that designs with larger pitch-to-width ratios tend to be more efficient but also more expensive.

The shape factor, π_2, impacts efficiency and cost in distinct ways. Fig. 5b illustrates that efficiency decreases as the shape factor increases, meaning that more elongated fields relative to receiver height negatively affect optical performance. However, the relationship between π_2 and cost is more complex, as seen in Fig. 5e. There are two obvious trends: one set of solutions shows small variations in π_2 but significant cost differences, which correspond to the vertical asymptotic trend observed in Fig. 3a. Another set of solutions maintains nearly constant costs while π_2 increases, representing the horizontal asymptotic behavior seen in Fig. 3a. This suggests that while some geometric variations lead to notable cost changes, others have minimal impact, depending on how mirror proportions are optimized relative to field layout.

Furthermore, considering now a metric for the specific cost of energy, $E = \Gamma / (ECF \cdot \sum I_b)$, Fig. 5 shows that π_1, π_2, and π_3 affect E similarly as Γ. That is, E decreases as π_1 increases, and the opposite occur as π_3 and π_2 increase. Minimum values of E in Fig. 5 are 0.078 and 0.08 €/kWh for NUN and VAR configurations, respectively, meaning that the full non-uniform case (NUN) yields a specific cost of energy 2.56 % lower than the variable radius configuration (VAR). This result agrees well with the impact of non-uniform settings regarding width and shift found by Boito and Grena [25] for an analogous metric.

Overall, these results highlight that increasing π_1 leads to cost reductions but with efficiency penalties, particularly for trivial solutions. The pitch factor, $\pi_3 = s/w$, directly influences both objectives, with higher values leading to more efficient but expensive configurations. Meanwhile, the shape factor, π_2, primarily affects efficiency, with cost dependencies varying across different design configurations. These insights reinforce the need for careful optimization of geometric parameters to balance cost and efficiency.

3.2. Curvature radius analysis

The currently approaches to design the curvature radius of primary mirrors [19,20,34,35] have an underlying assumption that such decision variable can be optimized in a step after the others (w, s, H_R). This assumption leads to the question: can the curvature radius be decoupled of other decision variables in design optimization?

To verify such a hypothesis, Fig. 6 presents a Pareto front comparison between two non-uniform configurations. One (NUN) have all primary mirror parameters (w, g, and R) subjected to optimization. The other configuration (NUN sunRef) is similar to the first one but now the curvature radius (R) is determined by the sun reference criterion [19,35] instead of being subject to optimization. Results are presented for two sizes of primary fields, (a) $n = 12$ and (b) $n = 25$, following a similar structure to the previous case. These results show that the two configurations produce nearly identical Pareto fronts, for primary fields with 12 and 25 mirrors, Fig. 6a and Fig. 6b, respectively, suggesting that determining the curvature radius by the sun reference criterion does not substantially alter the cost-efficiency trade-off.

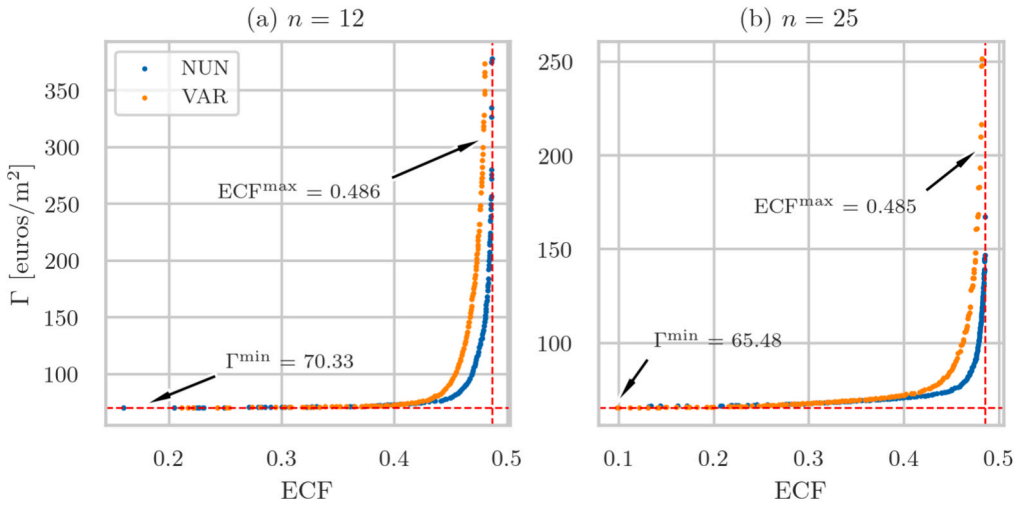

Fig. 3. Pareto Fronts of optimal solutions for non-uniform (NUN) and variable radius (VAR) designs, considering geometries for primary fields with (a) 12 and (b) 25 mirrors.

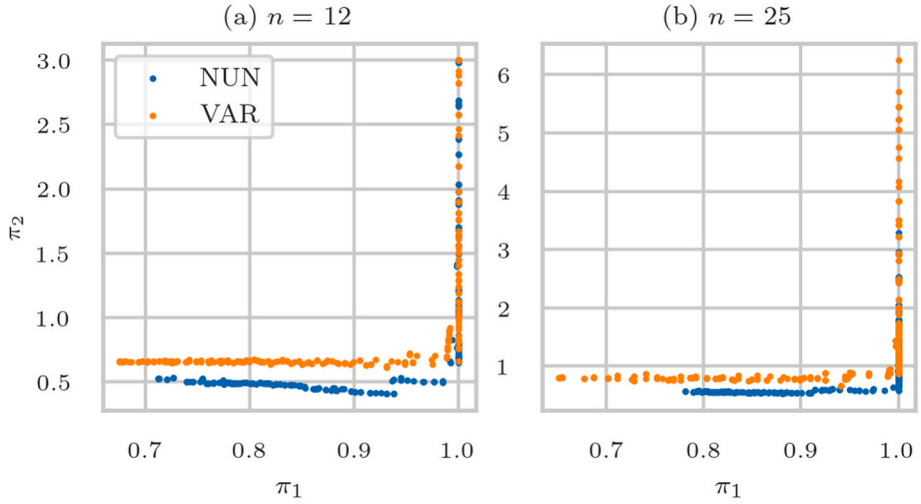

Fig. 4. Dispersion plots of dimensionless parameters showing the correlation between filling (π_1) and shape (π_2) factors, for (a) $n = 12$ and (b) $n = 25$. Each dot represents a Pareto solution shown in Fig. 3.

On the other hand, while the objective space analysis provides insights into the trade-offs between efficiency and cost, it does not reveal how different design variables contribute to these optimal solutions. In this sense, Fig. 7 presents the frequency distribution of decision variables for all Pareto solutions in Fig. 6a ($n = 12$), comparing the NUN and NUN sunRef configurations and providing insights into the distribution of key geometric parameters. It reveals strong similarities between NUN and NUN-sunRef configurations. The observed frequency trends highlight that design parameters remain across both configurations while maintaining comparable performance. These results highlight the effectiveness of the sun reference criterion in approximating optimized solutions.

This curvature design analysis can also be done regarding uniform configurations. As previously stated, the UN case defines a full uniform configuration, in which all decision variables (w, g, and R) are subjected to the optimization routine. The UN-IpaRef stands for a uniform configuration in which R is calculated by the criteria proposed by Pulido-Iparraguirre et al. [54] instead of subjected to the optimization routine. The comparison between UN and UN-IpaRef is presented in Fig. 8. These results shows that the two configurations produce nearly identical Pareto fronts, for primary fields with 12 and 25 mirrors, Fig. 8a and Fig. 8b, respectively, suggesting that determining the curvature radius by Iparraguirre's criterion does not substantially alter the cost-efficiency trade-off.

Regarding to the design space, Fig. 9 shows that UN and UN-IpaRef designs produce Pareto solutions with similar frequency distribution of geometric parameters. The higher differences are seen for the curvature radius R. Nevertheless, these differences does not have a major impact on performance, as both designs yield the same Pareto front. Of course, some small differences can be attributed to the stochastic nature NSGA-II in determining the decision variables of candidate solutions.

In short, the results presented in this section corroborates the hypothesis that the curvature radius can be decoupled from the optimization routine. This statement implies simplifying the linear Fresnel design problem, as a lower number of decision variables can be used without converging to local optimal solutions.

4. Conclusions

This work addressed the optimal design problem for linear Fresnel collectors by employing a two-objective optimization approach. The optimization was based on maximizing annual energy efficiency, while minimizing the specific direct cost of the solar field. The analysis compared Pareto-optimal solutions of different design configurations,

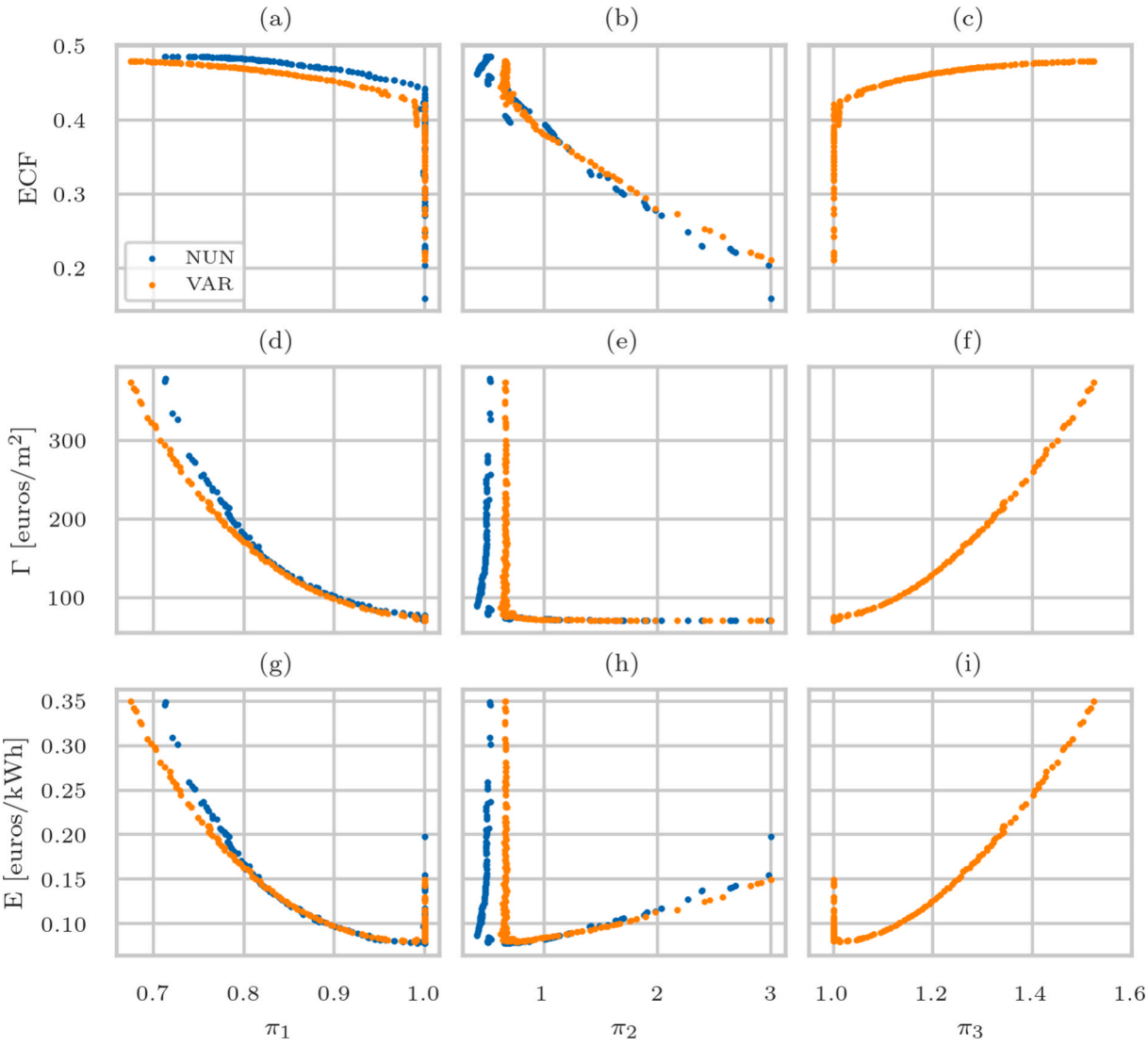

Fig. 5. Dimensionless parameters versus objective functions for both non-uniform (NUN) and variable radius (VAR) designs for primary fields with $n = 12$ mirrors. It shows how dimensionless parameters affect the specific cost of energy, $E = \Gamma/(ECF \cdot \sum I_b)$, in figures (g), (h), and (i).

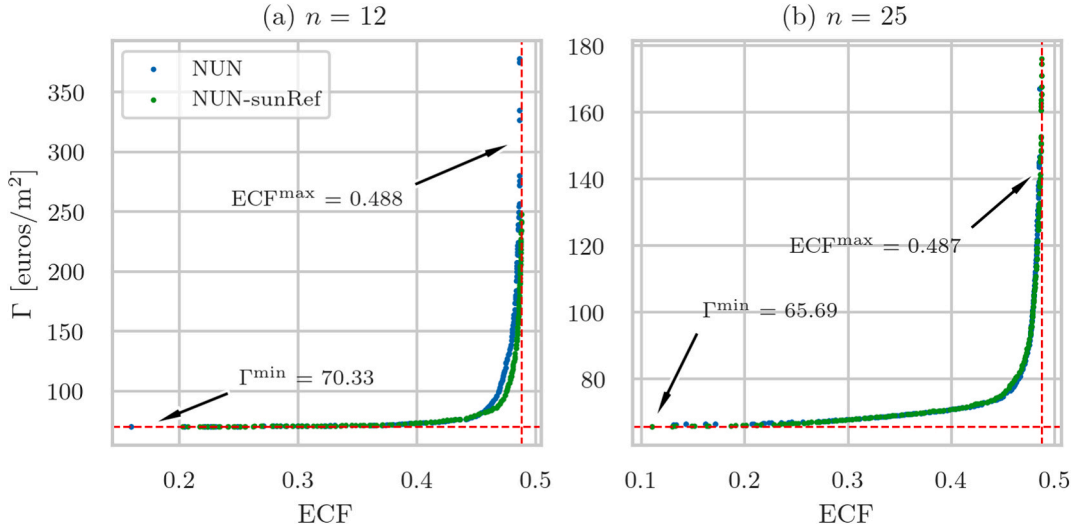

Fig. 6. Pareto solutions for two non-uniform configurations. The NUN-sunRef considers the curvature radius by the sun reference criterion instead of subjected to the optimization algorithm.

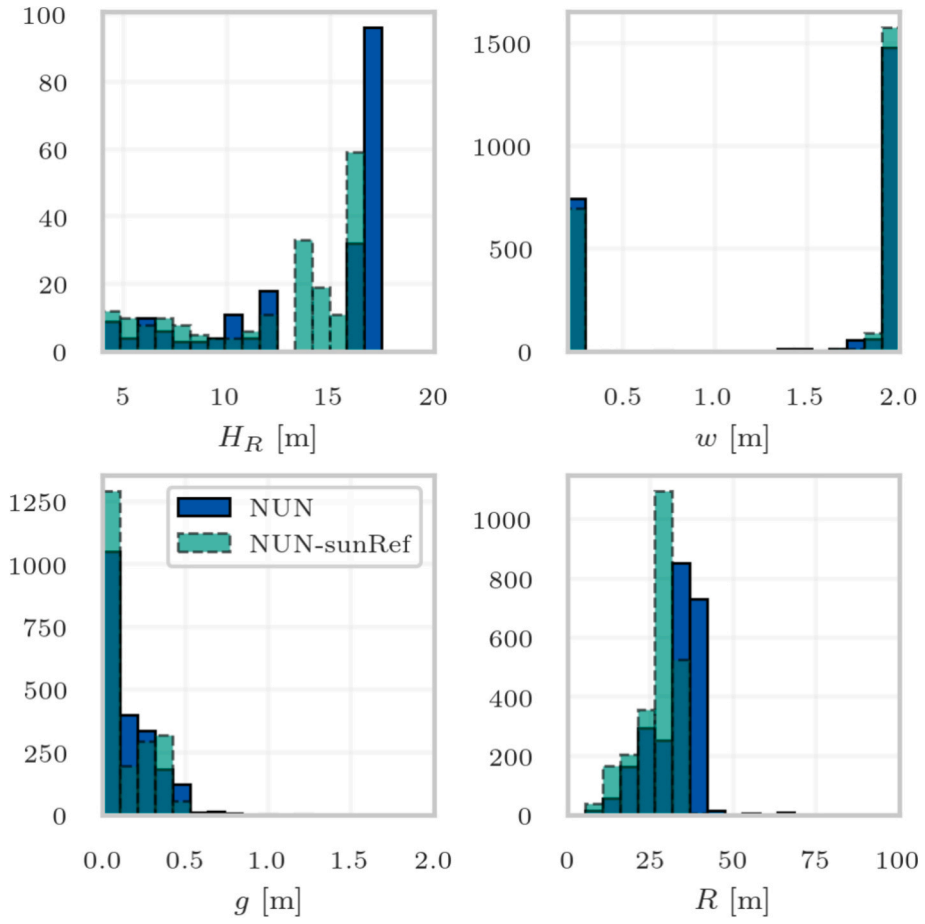

Fig. 7. Frequency distribution of decision variables for all Pareto solutions of NUN (blue) and NUN sunRef (green) configurations, for the case in which $n = 12$ mirrors. The histograms present terms of receiver height (H_R), mirror width (w), mirror gap (g), and curvature radius (R). (For interpretation of the references to colour in this figure legend, the reader is referred to the web version of this article.)

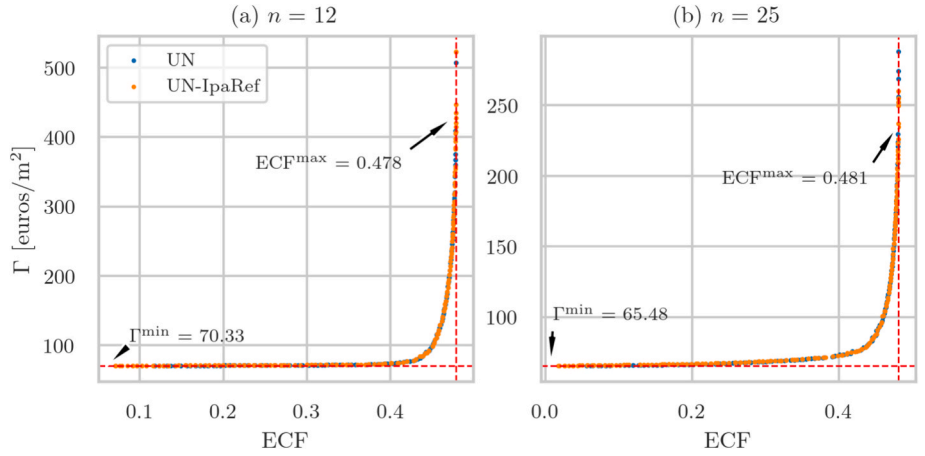

Fig. 8. Pareto solutions for two uniform configurations. The UN-IpaRef considers the curvature radius by Pulido-Iparraguirre's [54] criterion instead of subjected to the optimization algorithm.

particularly evaluating the cost-effectiveness of non-uniform designs (varying width, shift, and radius) relative to variable radius configurations (constant width and shift), and exploring whether the curvature radius can be effectively decoupled from other design variables.

The results obtained demonstrate that non-uniform designs can indeed be more cost-effective solutions. In certain regions of the objective space, differences between Pareto solutions for these two configurations are minimal, even excluding trivial cases. However, other regions indicate a clear cost advantage for non-uniform designs over variable radius cases. Additionally, Pareto solutions display considerable geometric diversity but also reveal identifiable trends when evaluated through dimensionless parameters.

The analysis of curvature radius suggests that predefined design criteria on non-uniform and uniform configurations (such as sun reference or Iparraguirre's model) yield solutions nearly identical to those obtained via optimization. Thus, curvature radius can effectively be

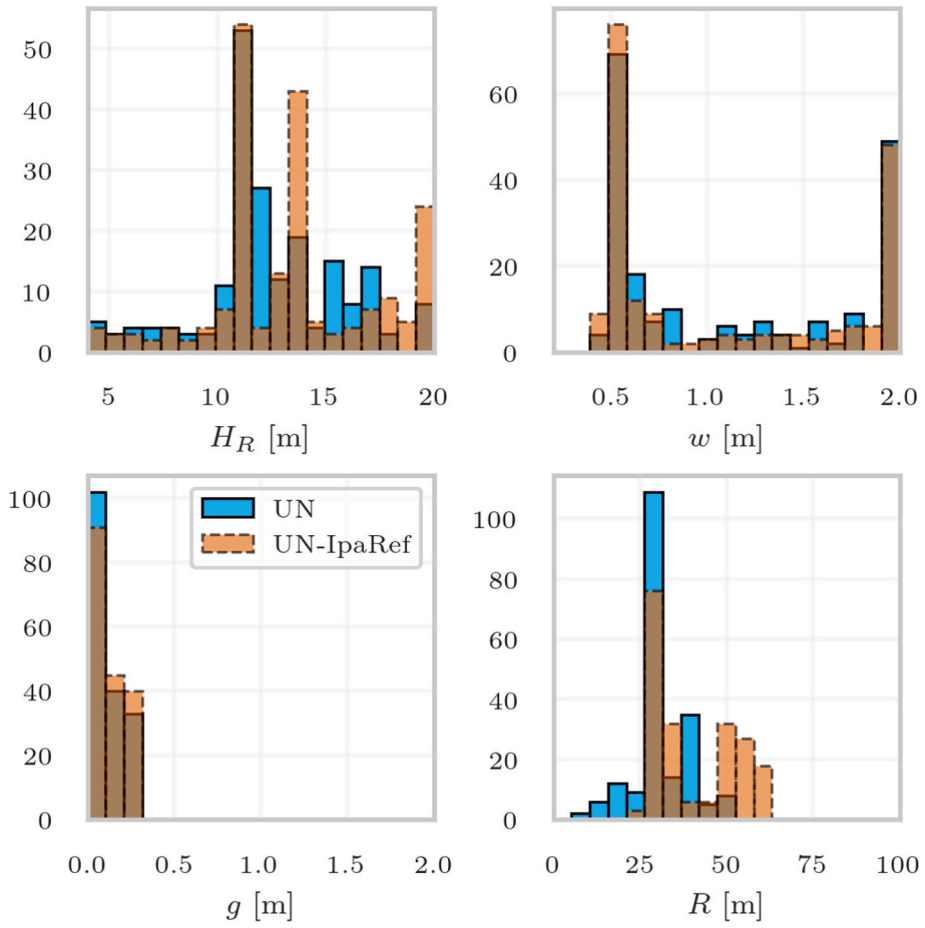

Fig. 9. Frequency distribution of decision variables for all Pareto solutions of UN (blue) and UN-IpaRef (orange) configurations, for the case in which $n = 25$ mirrors. The histograms presents terms of receiver height (H_R), mirror width (w), mirror gap (g), and curvature radius (R). (For interpretation of the references to colour in this figure legend, the reader is referred to the web version of this article.)

decoupled from other optimization variables without significantly compromising performance. Given the computational demands associated with optimization routines, these criteria represent practical alternatives for determining the curvature radius of mirrors while preserving optimal cost-performance.

It is worth noting that, by definition, Pareto solutions show the trade-off between the objectives, meaning that all of them are somehow equivalent and there is no single optimal solution. Therefore, the selection of a single case of a Pareto front ultimately depend on the user's choices, criteria, and considerations, and on what they value most. The results presented in this work provide insights into this design problem, establishing boundaries and limits but do not definitively determining the "best" solution.

These findings have implications beyond academic research, not only contributing new insights into the design problem but also offering practical tools and strategies for the optimization of linear Fresnel collectors. The marginal advantage of non-uniform designs is observed only within a specific range of the objective space, suggesting that under certain constraints – such as efficiency, cost, or other design criteria – the cost-effectiveness of this approach may be comparable to that of variable-radius designs, which involve a significantly simpler geometric configuration. Furthermore, decoupling the curvature radius from the optimization process streamlines the procedure by substantially reducing the number of decision variables involved. By presenting simplified yet robust design methodologies, these results enables engineers and designers to make informed decisions with reduced reliance on computational resources, particularly when establishing an initial, near-optimal geometric configuration as a basis for detailed engineering design subjected to subsequent cost optimization.

On the other hand, the assessment presented in this work assumes that the optical efficiency of the receiver remains approximately constant despite variations in transversal and longitudinal incidence angles, as well as across different edge-ray CECs. In other words, the ratio of absorbed flux to the flux entering the secondary aperture is considered invariant under these conditions, making the aperture flux a sufficient metric for identifying the configuration with the higher yield. This simplification represents a key modeling assumption which, while useful, may not hold in all cases and therefore requires validation – a subject to be addressed in future research.

Additionally, it should be noted that the findings and discussions in this paper rely on the cost model outlined in Section 2.2.2. This model excludes considerations such as the impact of curvature radius and effects of various non-uniform configurations on direct specific const of the solar field, as well as on capital and operational expenditures – a clearly defined limitation within the scope of this work. Consequently, alternative cost models might yield different conclusions regarding the established research questions.

Therefore, developing more comprehensive and accurate cost models for linear Fresnel collectors is essential for a deeper assessment of geometric configurations and to verify hypotheses regarding the simplification of design problems – another subject to be addressed in future research. Nevertheless, given the currently limited commercial maturity of linear Fresnel power plants, the scarcity of data presents a substantial challenge to advancing such models.

CRediT authorship contribution statement

André Vitor Santos: Writing – review & editing, Writing – original draft, Visualization, Validation, Software, Methodology, Investigation, Formal analysis, Data curation, Conceptualization. **Diogo Canavarro:** Writing – review & editing, Writing – original draft, Validation, Supervision, Project administration, Methodology. **Pedro Horta:** Writing – review & editing, Writing – original draft, Validation, Supervision, Project administration, Methodology. **Manuel Collares-Pereira:** Writing – review & editing, Writing – original draft, Validation, Supervision, Methodology.

Declaration of competing interest

The authors declare that they have no known competing financial interests or personal relationships that could have appeared to influence the work reported in this paper.

Acknowledgments

Author André Santos acknowledge the financial support by the *Fundação para a Ciência e a Tecnologia* through the Ph.D. scholarship 2021.07140.BD[1].

References

[1] W.J. Platzer, D. Mills, W. Gardner, Linear Fresnel Collector (LFC) solar thermal technology, in: Concentrating Solar Power Technology, Elsevier, 2021: pp. 165–217. doi:10.1016/B978-0-12-819970-1.00006-2.
[2] M. Collares-Pereira, D. Canavarro, J. Chaves, Improved design for linear Fresnel reflector systems, in: M.J. Blanco, L.R. Santigosa (Eds.), Advances in Concentrating Solar Thermal Research and Technology, Elsevier, 2017, pp. 45–55, https://doi.org/10.1016/B978-0-08-100516-3.00003-4.
[3] A.V. Santos, D. Canavarro, P. Horta, M. Collares-Pereira, On the comparison of parabolical and cylindrical primary mirrors for linear Fresnel solar concentrators, Renew. Energy 218 (2023) 119380, https://doi.org/10.1016/j.renene.2023.119380.
[4] G. Morin, J. Dersch, W. Platzer, M. Eck, A. Häberle, Comparison of linear fresnel and parabolic trough collector power plants, Sol. Energy 86 (2012) 1–12, https://doi.org/10.1016/j.solener.2011.06.020.
[5] A. Giostri, M. Binotti, P. Silva, E. Macchi, G. Manzolini, Comparison of two linear collectors in solar thermal plants: parabolic trough versus fresnel, J. Sol. Energy Eng. 135 (2012) 011001, https://doi.org/10.1115/1.4006792.
[6] H. Schenk, T. Hirsch, J. Fabian Feldhoff, M. Wittmann, Energetic comparison of linear fresnel and parabolic trough collector systems, J. Sol. Energy Eng. 136 (2014) 04101501–04101511, https://doi.org/10.1115/1.4027766.
[7] R. Abbas, M.J. Montes, A. Rovira, J.M. Martínez-Val, Parabolic trough collector or linear Fresnel collector? a comparison of optical features including thermal quality based on commercial solutions, Solar Energy. 124 (2016) 198–215, https://doi.org/10.1016/j.solener.2015.11.039.
[8] N. Kincaid, G. Mungas, N. Kramer, M. Wagner, G. Zhu, An optical performance comparison of three concentrating solar power collector designs in linear Fresnel, parabolic trough, and central receiver, Appl. Energy 231 (2018) 1109–1121, https://doi.org/10.1016/J.APENERGY.2018.09.153.
[9] D.R. Mills, G.L. Morrison, Compact linear fresnel reflector solar thermal powerplants, Sol. Energy 68 (2000) 263–283, https://doi.org/10.1016/S0038-092X(99)00068-7.
[10] J. Chaves, M. Collares-Pereira, Etendue-matched two-stage concentrators with multiple receivers, Sol. Energy 84 (2010) 196–207, https://doi.org/10.1016/j.solener.2009.10.022.
[11] A. Vouros, E. Mathioulakis, E. Papanicolaou, V. Belessiotis, Performance evaluation of a linear Fresnel collector with catoptric subsets, Renew. Energy 156 (2020) 68–83, https://doi.org/10.1016/j.renene.2020.04.062.
[12] J. Cano-Nogueras, J. Muñoz-Antón, J.M. Martinez-Val, A new thermal-solar field configuration: the rotatory fresnel collector or sundial, Energies 14 (2021) 4139, https://doi.org/10.3390/en14144139.
[13] M. Barnetche, L.F. González-Portillo, M. Ibarra, R. Barbero, A. Rovira, R. Abbas, Dynamic analysis of the SunDial, the rotatory Fresnel collector, in: SolarPACES: SOLAR POWER & CHEMICAL ENERGY SYSTEMS: 27th International Conference on Concentrating Solar Power and Chemical Energy Systems, 27 September–1 October 2021, 2023: p. 140002. doi:10.1063/5.0149992.
[14] D. Canavarro, J. Chaves, M. Collares-Pereira, Simultaneous Multiple Surface method for Linear Fresnel concentrators with tubular receiver, Sol. Energy 110 (2014) 105–116, https://doi.org/10.1016/j.solener.2014.09.002.
[15] D. Canavarro, J. Chaves, M. Collares-Pereira, New dual asymmetric CEC linear Fresnel concentrator for evacuated tubular receivers, in, AIP Conf. Proc. (2017) 040001, https://doi.org/10.1063/1.4984397.
[16] A. Sánchez-González, J. Gómez-Hernández, Beam-down linear Fresnel reflector: BDLFR, Renew. Energy 146 (2020) 802–815, https://doi.org/10.1016/j.renene.2019.07.017.
[17] L.F.L. de Souza, N. Fraidenraich, C. Tiba, J.M. Gordon, Linear aplanatic Fresnel reflector for practical high-performance solar concentration, Sol. Energy 222 (2021) 259–268, https://doi.org/10.1016/j.solener.2021.05.002.
[18] R. Abbas, M.J. Montes, M. Piera, J.M. Martínez-Val, Solar radiation concentration features in Linear Fresnel Reflector arrays, Energ. Conver. Manage. 54 (2012) 133–144, https://doi.org/10.1016/j.enconman.2011.10.010.
[19] R. Abbas, J.M. Martínez-Val, Analytic optical design of linear Fresnel collectors with variable widths and shifts of mirrors, Renew. Energy 75 (2015) 81–92, https://doi.org/10.1016/j.renene.2014.09.029.
[20] R. Abbas, J.M. Martínez-Val, A comprehensive optical characterization of linear Fresnel collectors by means of an analytic study, Appl. Energy 185 (2017) 1136–1151, https://doi.org/10.1016/j.apenergy.2016.01.065.
[21] R. Abbas, M. Valdés, M.J. Montes, J.M. Martínez-Val, Design of an innovative linear Fresnel collector by means of optical performance optimization: a comparison with parabolic trough collectors for different latitudes, Sol. Energy 153 (2017) 459–470, https://doi.org/10.1016/j.solener.2017.05.047.
[22] J.D. Nixon, P.A. Davies, Cost-exergy optimisation of linear Fresnel reflectors, Sol. Energy 86 (2012) 147–156, https://doi.org/10.1016/j.solener.2011.09.024.
[23] M.J. Montes, C. Rubbia, R. Abbas, J.M. Martínez-Val, A comparative analysis of configurations of linear Fresnel collectors for concentrating solar power, Energy 73 (2014) 192–203, https://doi.org/10.1016/j.energy.2014.06.010.
[24] A.V. Santos, D. Canavarro, M. Collares-Pereira, The gap angle as a design criterion to determine the position of linear Fresnel primary mirrors, Renew. Energy 163 (2021) 1397–1407, https://doi.org/10.1016/j.renene.2020.09.017.
[25] P. Boito, R. Grena, Optimization of the geometry of Fresnel linear collectors, Sol. Energy 135 (2016) 479–486, https://doi.org/10.1016/j.solener.2016.05.060.
[26] M.A. Moghimi, K.J. Craig, J.P. Meyer, Simulation-based optimisation of a linear Fresnel collector mirror field and receiver for optical, thermal and economic performance, Sol. Energy 153 (2017) 655–678, https://doi.org/10.1016/J.SOLENER.2017.06.001.
[27] Z.D. Cheng, X.R. Zhao, Y.L. He, Y. Qiu, A novel optical optimization model for linear Fresnel reflector concentrators, Renew. Energy 129 (2018) 486–499, https://doi.org/10.1016/j.renene.2018.06.019.
[28] H. Ajdad, Y. Filali Baba, A. Al Mers, O. Merroun, A. Bouatem, N. Boutammachte, Particle swarm optimization algorithm for optical-geometric optimization of linear fresnel solar concentrators, Renew. Energy 130 (2019) 992–1001, https://doi.org/10.1016/j.renene.2018.07.001.
[29] O.A. López-Núñez, J.A. Alfaro-Ayala, J.J. Ramírez-Minguela, J.M. Belman-Flores, O.A. Jaramillo, Optimization of a linear fresnel reflector applying computational fluid dynamics, entropy generation rate and evolutionary programming, Renew. Energy 152 (2020) 698–712, https://doi.org/10.1016/j.renene.2020.01.105.
[30] J.-J. Men, X.-R. Zhao, Z.-D. Cheng, Y.-K. Leng, Y.-L. He, Study on the annual optical comprehensive performance of linear Fresnel reflector concentrators with an effective multi-objective optimization model, Sol. Energy 225 (2021) 591–607, https://doi.org/10.1016/j.solener.2021.07.051.
[31] V. Sharma, J.K. Nayak, S.B. Kedare, Effects of shading and blocking in linear Fresnel reflector field, Sol. Energy 113 (2015) 114–138, https://doi.org/10.1016/j.solener.2014.12.026.
[32] A. Ahmadpour, A. Dejamkhooy, H. Shayeghi, Optimization and modelling of linear Fresnel reflector solar concentrator using various methods based on Monte Carlo Ray–Trace, Sol. Energy 245 (2022) 67–79, https://doi.org/10.1016/j.solener.2022.09.006.
[33] J. Song, J. Ma, Z. Zhan, Y. Dai, Optical Analysis and Optimization of the Linear Fresnel Collector's Mirror Field, in: Proceedings of the 2015 International Forum on Energy, Environment Science and Materials, Atlantis Press, Paris, France, 2015: pp. 474–478. doi:10.2991/ifeesm-15.2015.90.
[34] P. Boito, R. Grena, Optimal focal length of primary mirrors in Fresnel linear collectors, Sol. Energy 155 (2017) 1313–1318, https://doi.org/10.1016/j.solener.2017.07.079.
[35] A.V. Santos, D. Canavarro, P. Horta, M. Collares-Pereira, Assessment of the optimal curvature radius of linear Fresnel primary mirrors, Sol. Energy 270 (2024) 112376, https://doi.org/10.1016/j.solener.2024.112376.
[36] S. Teske, J. Leung, L. Crespo, M. Bial, E. Dufour, C. Richter, Solar thermal Electricity - Global Outlook 2016, European Solar Thermal Electricity Association (ESTELA), Brussels, 2016.
[37] M. Collares-Pereira, D. Canavarro, L.L. Guerreiro, Linear Fresnel reflector (LFR) plants using superheated steam, molten salts, and other heat transfer fluids, in: M. J. Blanco, L.R. Santigosa (Eds.), Advances in Concentrating Solar Thermal Research and Technology, Elsevier, Cham, 2017, pp. 339–352, https://doi.org/10.1016/B978-0-08-100516-3.00015-0.
[38] RioGlass, Receiver tubes for linear csp (concentrated solar power) applications, (n. d.). https://www.rioglass.com/en/our-products/hce-tubes (accessed August 23, 2023).
[39] F. Burkholder, C. Kutscher, Heat Loss Testing of Schott's 2008 PTR70 Parabolic Trough Receiver, Golden, CO (United States), 2009. doi:10.2172/1369635.
[40] M. Cagnoli, D. Mazzei, M. Procopio, V. Russo, L. Savoldi, R. Zanino, Analysis of the performance of linear Fresnel collectors: Encapsulated vs. evacuated tubes, Sol. Energy 164 (2018) 119–138, https://doi.org/10.1016/j.solener.2018.02.037.
[41] A. Santos, D. Canavarro, C.A. Arancibia-Bulnes, P. Horta, M. Collares-Pereira, A comparison of secondary optic designs for linear Fresnel collectors with a single

[1] https://doi.org/10.54499/2021.07140.BD.

tubular absorber, Sol. Energy 282 (2024) 112936, https://doi.org/10.1016/j.solener.2024.112936.
[42] J. Chaves, Introduction to Nonimaging Optics, 2nd ed., CRC Press, New York, 2017, 10.1201/b18785.
[43] A.V. Santos, D. Canavarro, P. Horta, M. Collares-Pereira, An analytical method for the optical analysis of Linear Fresnel Reflectors with a flat receiver, Sol. Energy 227 (2021) 203–216, https://doi.org/10.1016/j.solener.2021.08.085.
[44] W.F. Holmgren, C.W. Hansen, M.A. Mikofski, pvlib python: a python package for modeling solar energy systems, J. Open Source Software 3 (2018) 884, https://doi.org/10.21105/joss.00884.
[45] I. Reda, A. Andreas, Solar position algorithm for solar radiation applications, Sol. Energy 76 (2004) 577–589, https://doi.org/10.1016/j.solener.2003.12.003.
[46] W.R. McIntire, Factored approximations for biaxial incident angle modifiers, Sol. Energy 29 (1982) 315–322, https://doi.org/10.1016/0038-092X(82)90246-8.
[47] R. Bernhard, S. Hein, J. LaLaing, M. Eck, M. Eickhoff, M. Pfaender, G. Morin, A. Häberle, Linear Fresnel collector demonstration on the PSA Part II - commissioning and first performance tests. In: 14th International Symposium on Concentrated Solar Power and Chemical Energy Technologies, 2008.
[48] J.D. Hertel, V. Martinez-Moll, R. Pujol-Nadal, Estimation of the influence of different incidence angle modifier models on the biaxial factorization approach, Energ. Conver. Manage. 106 (2015) 249–259, https://doi.org/10.1016/j.enconman.2015.08.082.
[49] M. Shokrnia, M. Cagnoli, R. Grena, A. D'Angelo, M. Lanchi, R. Zanino, Comparative techno-economic analysis of parabolic trough and linear fresnel collectors with evacuated and non-evacuated receiver tubes in different geographical regions, Processes 12 (2024) 2376, https://doi.org/10.3390/pr12112376.
[50] M. Cagnoli, M. Shokrnia, R. Zanino, Analisi delle prestazioni termiche di ricevitori con coating selettivi a bassa emissività applicati a tubi ricevitori evacuati operanti fino a 550 ° C, 2020. https://www2.enea.it/it/Ricerca_sviluppo/documenti/ricerca-di-sistema-elettrico/adp-mise-enea-2019-2021/solare-termodinamico/report-rds_ptr_2020_262.pdf.
[51] M. Mertins, Technische und wirtschaftliche Analyse von horizontalen Fresnel-Kollektoren, University of Karlsruhe, 2009. PhD Thesis.
[52] T. Hirsch, E. Yildiz, F. Hustig-Diethelm, S. Heide, J. Kretschmann, CSP Bankability Project Report Draft: Draft for an Appendix O – Cost Structures to the SolarPACES Guideline for Bankable STE Yield Assessment, (2017). https://shorturl.at/57MDO.
[53] D. Pulido-Iparraguirre, L. Valenzuela, J. Fernández-Reche, J. Galindo, J. Rodríguez, Design, manufacturing and characterization of linear fresnel reflector's facets, Energies 12 (2019) 2795, https://doi.org/10.3390/en12142795.
[54] D. Pulido-Iparraguirre, L. Valenzuela, J.-J. Serrano-Aguilera, A. Fernández-García, Optimized design of a Linear Fresnel reflector for solar process heat applications, Renew. Energy 131 (2019) 1089–1106, https://doi.org/10.1016/j.renene.2018.08.018.
[55] J.R.R.A. Martins, A. Ning, Engineering Design Optimization, Cambridge University Press, 2021, 10.1017/9781108980647.
[56] M.J. Kochenderfer, T.A. Wheeler, Algorithms for optimization, MIT Press, Cambridge, 2019 https://algorithmsbook.com/optimization/.
[57] K. Deb, Multi-Objective Optimization using Evolutionary Algorithms, John Wiley & Sons, New York, 2001.
[58] K. De Jong, Evolutionary Computation: a Unified Approach, The MIT Press, Cambridge, 2006 https://mitpress.mit.edu/books/evolutionary-computation.
[59] A.E. Eiben, J.E. Smith, Introduction to Evolutionary Computing, 2nd Ed.,, Springer Berlin Heidelberg, Berlin, Heidelberg, 2015, 10.1007/978-3-662-44874-8.
[60] F.-A. Fortin, F.-M. De Rainville, M.-A. Gardner, M. Parizeau, C. Gagné, DEAP: evolutionary algorithms made easy, J. Mach. Learn. Res. 13 (2012) 2171–2175. https://github.com/deap/deap.
[61] K. Deb, S. Agrawal, A. Pratap, T. Meyarivan, A Fast Elitist Non-dominated Sorting Genetic Algorithm for Multi-objective Optimization: NSGA-II, in: CEUR Workshop Proceedings, 2000: pp. 849–858. doi:10.1007/3-540-45356-3_83.